Image Separation with Side Information: A Connected Auto-Encoders Based Approach

Wei Pu, Barak Sober, Nathan Daly, Chao Zhou, Zahra Sabetsarvestani, Catherine Higgitt, Ingrid Daubechies, and Miguel R.D. Rodrigues.

***Abstract*—X-radiography (X-ray imaging) is a widely used imaging technique in art investigation. It can provide information about the condition of a painting as well as insights into an artist's techniques and working methods, often revealing hidden information invisible to the naked eye. X-radiograpy of double-sided paintings results in a mixed X-ray image and this paper deals with the problem of separating this mixed image. Using the visible color images (RGB images) from each side of the painting, we propose a new Neural Network architecture, based upon 'connected' auto-encoders, designed to separate the mixed X-ray image into two simulated X-ray images corresponding to each side. This connected auto-encoders architecture is such that the encoders are based on convolutional learned iterative shrinkage thresholding algorithms (CLISTA) designed using algorithm unrolling techniques, whereas the decoders consist of simple linear convolutional layers; the encoders extract sparse codes from the visible image of the front and rear paintings and mixed X-ray image, whereas the decoders reproduce both the original RGB images and the mixed X-ray image. The learning algorithm operates in a totally self-supervised fashion without requiring a sample set that contains both the mixed X-ray images and the separated ones. The methodology was tested on images from the double-sided wing panels of the *Ghent Altarpiece*, painted in 1432 by the brothers Hubert and Jan van Eyck. These tests show that the proposed approach outperforms other state-of-the-art X-ray image separation methods for art investigation applications.**

***Index Terms*—Image separation, image unmixing, deep neural networks, convolutional neural networks, auto-encoders, side information**

I. Introduction

OLD Master paintings – precious objects illuminating Europe's rich cultural heritage and history – are often the subject of detailed technical examination, whether to investigate an artist's materials and technique or in support of conservation or restoration treatments in order to preserve them for future generations. These processes have traditionally relied on X-ray radiography (or X-ray imaging) [1], infrared reflectography [2] or micro-sample analysis [3] – an invasive and destructive process – in order to understand the materials present within specific features of a painting [4], [5].

W. Pu, C. Zhou, Z. Sabetsarvestani and M. R.D. Rodrigues are with the Department of Electronic and Electrical Engineering, University College London, UK. Z. Sabetsarvestani is also with the American International Group, UK. B. Sober is with the Department of Mathematics and Rhodes Information Initiative, Duke University, US. N. Daly and C. Higgitt are with the Scientific Department, National Gallery, London, UK. I. Daubechies is with the Department of Electrical and Computer Engineering, Department of Mathematics, and Rhodes Information Initiative, Duke University, US.

This work is sponsored by Engineering and Physical Sciences Research Council (Ref. EP/R032785/1) and the Royal Society (Ref. NIF/R1/180735).

More recently, to complement these traditional approaches to the technical study of works of art, the cultural heritage sector has been gradually witnessing the increased use of non-invasive and non-destructive, cutting-edge analytical and imaging techniques and generating large and typically multi-dimensional datasets associated with artwork [6]–[8]. Such techniques include macro X-ray fluorescence (MA-XRF) scanning [9]–[11] and hyperspectral imaging [12]–[15]. Sophisticated multimodal image and data processing tools have been developed to exploit these new datasets and the increasingly high-resolution digital images now available using more traditional imaging techniques (e.g. X-ray imaging, infrared reflectography and various forms of multispectral imaging [13]) to tackle various challenging tasks arising in the field of art investigation [16], [17], such as crack detection [18], [19], material identification [20]–[23], brush stroke style analysis [24]–[27], canvas pattern or stretcher bar removal [28]–[30], automated canvas weave analysis [31], [32], and improved visualization of concealed features or under-drawing [12], [33]–[36].

Due to the ability of X-rays to penetrate deep into a painting's stratigraphy, X-radiographs (X-ray images) are especially important during the examination and restoration of paintings [1], [37], [38]. They can help to establish the condition of a painting (e.g., losses and damages not apparent at the surface) and the status of different paint passages (e.g., to identify retouchings, fills or other conservation interventions). X-ray images can also provide insights into an artist's technique and working methods, for example revealing the painting's stratigraphy (the buildup of the different paint layers which may include concealed earlier designs or pentimenti), and information about the painting support (e.g., type of canvas or the construction of a canvas or panel) or even some indication of the pigments used. However, where a support is painted on both the front and reverse sides, the resulting X-ray image of the painting will inevitably contain a mix or blend of the features associated with the paint application on each side (including any design changes, areas of damage, etc). In addition, the X-ray image of a double-sided painting will include other features associated with support for the painting (e.g., nails and battens, wood grain, stretcher bars, etc.). As the resulting mixed X-ray images - which are 2D representations of 3D works of art - are difficult for even experts to interpret, it is relevant to devise approaches that can separate such a mixed X-ray image into (hypothetical) constituent images, corresponding to the various component features. Typically, the mixed X-ray images are separated

into two images, associated with each side of the double-sided painting, with any (typically minor) contributions from the painting support being divided between the two resultant images. While a mixed X-ray image could potentially be divided into two images associated with the two paintings and a third associated with the support, the separating of the mixed image into just two resultant images should ensure that all of the highly informative detail about the surface and sub-surface features of the paint layers on a given side of the painting remain associated within a single image.

The task of separating mixed signals has been studied extensively in the blind source separation (BSS) and the informed source separation (ISS) literature. Among the approaches designed to tackle this challenge, we can mention independent component analysis (ICA) [39], [40], robust principal component analysis (PCA) [41]–[43] and morphological component analysis (MCA) [44]–[46]. These methods often rely on some strong prior assumptions including independence, sparsity or low-rankness. However, the implementation of such techniques in art investigation applications is generally problematic because such typical prior assumptions adopted by other methods do not always hold.

Recently, deep learning architectures have also been successfully applied to various signal and image separation challenges [47]–[50]. Such approaches typically fall into three different categories: unsupervised, semi-supervised and supervised approaches. The supervised case typically assumes one has access to a training dataset containing a number of examples of mixed and associated component signals that can be used to train a deep neural network carrying out the separation task [47], [48]. In contrast, in the unsupervised case one does not have access to such a training dataset; instead, the sources are typically separated by minimizing joint adverse and remix losses as in [50]. Finally, in the semi-supervised case one may have access to samples of one individual source but not other sources; a neural egg separation (NES) method [49] integrated with generative adversarial networks (GANs) [51] has been recently proposed to tackle the semi-supervised source separation challenge. However, again, the application of these approaches to challenges associated with the unmixing of an X-ray image into its constituents can also be problematic since the data one typically has access to prevents the use of supervised or semi-supervised approaches.

Fig. 1. Two double-sided panels from the *Ghent Altarpiece* [52]: (left) visible RGB image of the front side, (centre) visible RGB image of the back side, (right) mixed X-ray image.

There are, however, various cases where one has access to both mixed X-ray images along with additional images that can potentially be exploited to aid in the image separation task. For example, in the separation of mixed X-ray images associated with double-sided paintings – such as the outer wing panels of the large polyptych *The Adoration of the Mystic Lamb*, painted by Hubert and Jan van Eyck and more commonly known as the *Ghent Altarpiece* [52]–[54], shown in Fig. 1 – one can also potentially use the visible (RGB or grayscale) images associated with both sides of the outer panels, in order to understand traits such as general contours, paint passages and losses to improve the separation.

A number of image processing approaches based on sparsity [55], Gaussian mixture models [57] or deep learning [56], [58] have been proposed to address such a challenge in the context of double-sided paintings. The approaches proposed in [55], [57], which exploited sparsity and Gaussian mixture models, have been partially successful, whereas the deep learning approaches in [56], [58] have led to signifi cantly better results. It should be noted that although X-ray images do contain physical meaning and will depend on the acquisition and processing parameters, to simplify the challenge of separating the mixed signals, they are typically considered as simple images.

In this paper, we propose another self-supervised learning approach to perform the separation of mixed X-ray images originating from double-sided paintings given the visible images associated with each side of the painting. Our approach is motivated by recent advances in algorithm unrolling techniques [59]. Moreover, our approach outperforms the state-of-the-art approaches designed to tackle this specific problem [56], [58].

Our main contributions can be summarized as follows:

- Firstly, we formulate the mixture model of the X-ray image based on the attenuation model of X-ray transmission. The novel X-ray mixture model makes the hypothesis of the proposed method more reasonable. With this theoretical basis, the novel X-ray mixture model can also lead to better results. Additionally, we also formulate the X-ray image separation problem with side information by leveraging a convolutional sparse coding model.
- Secondly, we decouple the X-ray image separation problem into three separate optimization problems, solve them using convolutional iterative thresholding (CISTA) algorithms, and unroll such solvers into deep neural networks.
- Thirdly, we recouple different networks into one overall network, resulting in a connected auto-encoder structure. The various auto-encoders are connected in the sparse feature maps and the auto-encoders for the RGB images of the front and rear paintings share the same weights.
- Fourthly, we also offer a detailed analysis of the effect of various regularization parameters associated with our separation method on performance.
- Finally, we apply our proposed approach to a real dataset, showcasing state-of-the-art results over competing methods. The dataset relates to images taken from the double-sided wing panels of the *Ghent Altarpiece* in Fig. 1.

The remainder of the paper is organized as follows: Section II overviews related work. Section III introduces our proposed approach. Section IV introduces our experimental results. Finally, Section V draws various conclusions. The dataset the *Ghent Altarpiece* is available at [52]. The code of the proposed approach and the other databases utilized in this paper are available at https://github.com/ChaoEdisonZhouUCL/Code.

II. Related work

Our work is inspired by the sparsity-driven image separation with side information approach put forth in [55], whose purpose is to separate a mixed X-ray image of a double-sided painting into its constituent X-ray images by leveraging the availability of the visible images, i.e., RGB or grayscale images, pertaining to the front and reverse of the painting.

Suppose x^v denotes a vectorized version of a mixed X-ray image patch; x_1^v and x_2^v denote the vectorized versions of the corresponding individual constituent X-ray image patches (corresponding to the front and back side paintings, respectively); and g_1^v and g_2^v denote the vectorized versions of the corresponding grayscale image patches (corresponding to the front and back side paintings, respectively).

The authors in [55] assume that the mixed X-ray signal is the sum of the individual X-ray signals as follows:

$$x^v = x_1^v + x_2^v \tag{1}$$

The authors also assume that the various signals obey a sparse representation under some given dictionaries as follows:

$$\begin{aligned} g_1^v &= \Phi_g z_1^v \\ g_2^v &= \Phi_g z_2^v \end{aligned} \tag{2}$$

and

$$\begin{aligned} x_1^v &= \Phi_x z_1^v + \Theta s^v \\ x_2^v &= \Phi_x z_2^v + \Theta s^v \end{aligned} \tag{3}$$

where z_1^v, z_2^v and s^v represent sparse vectors and Φ_g, Φ_x and Θ represent dictionaries. Note that this model is such that the sparse vectors z_1^v and z_2^v are common to the images in the grayscale and X-ray domains – capturing similarities between both individual modalities – whereas the sparse vector s^v is specific to the images in the X-ray domain in order to capture features specific to this image modality only.

The authors then propose to recover the individual X-ray image patches from a mixed X-ray patch and the individual grayscale image patches using a two-step approach as follows:

- Firstly, the various dictionaries associated with the model in (1) are learnt using a modified Orthogonal Matching Pursuit (OMP) algorithm, by using various image patches sampled from X-ray images and grayscale visual images sampled from single-sided panels.
- Secondly, the individual X-ray image patches are recovered from a mixed X-ray patch and the individual grayscale image patches using the sparse coding problem given by: [1]

$$\begin{aligned} \min_{z_1^v, z_2^v, s^v} \quad & \|z_1^v\|_1 + \|z_2^v\|_1 + 2\|s^v\|_1 \\ \text{s.t.} \quad & x^v = \Phi_x z_1^v + \Phi_x z_2^v + \Theta s^v \\ & g_1^v = \Phi_g z_1^v \\ & g_2^v = \Phi_g z_2^v. \end{aligned} \tag{4}$$

The estimated X-ray image patches $\hat{x}_1^v$ and $\hat{x}_2^v$ are then obtained from the estimated sparse representations $\hat{z}_1^v$, $\hat{z}_2^v$, and $\hat{s}^v$ as follows:

$$\begin{aligned} \hat{x}_1^v &= \Phi_x \hat{z}_1^v + \Theta \hat{s}^v \\ \hat{x}_2^v &= \Phi_x \hat{z}_2^v + \Theta \hat{s}^v \end{aligned} \tag{5}$$

Overall, this approach exhibits some limitations:

- Firstly, it deals with a vectorized version of the image patches rather than the image patches themselves, so it fails to capture two-dimensional information that might be relevant to improve separation.
- Secondly, it deals with the grayscale version of the visible images instead of the RGB version of the same images, so it also fails to capture color information that might be relevant to improve separation.
- Finally, the X-ray image separation still exhibits various artefacts [55], bearing further witness to the limitations of the method.

A similar approach – relying on Gaussian mixture models instead of sparsity based models – proposed in [57] also shares some of these limitations.

Some of these limitations have been recently partially addressed by relying on deep models in [56], [58]. In particular, let $x \in \mathbb{R}^{n_1 \times n_2}$ denote a mixed X-ray image patch, let $x_1 \in \mathbb{R}^{n_1 \times n_2}$ and $x_2 \in \mathbb{R}^{n_1 \times n_2}$ denote the hypothetical, separated X-ray image patches corresponding to the front and rear sides of the painting, respectively, and $r_1 \in \mathbb{R}^{n_1 \times n_2 \times 3}$ and $r_2 \in \mathbb{R}^{n_1 \times n_2 \times 3}$ denote the RGB visible image patches corresponding to the front and rear sides of the painting. Let also the mixed X-ray patch x be expressed in terms of the individual X-ray patches x_1 and x_2 as follows:

$$x \approx x_1 + x_2. \tag{6}$$

Reference [56] postulates the existence of a mapping function $\mathcal{F}(\cdot)$ that converts the RGB image patches r_1 and r_2 into the corresponding X-ray image patches. The mapping function $\mathcal{F}(\cdot)$ is modelled via a 7-layer convolutional neural network. This mapping function is then learnt in a completely self-supervised manner by solving the following optimization problem:

$$\min_{\mathcal{F}} \quad \|x - \mathcal{F}(r_1) - \mathcal{F}(r_2)\|_F . \tag{7}$$

where $\|\cdot\|_F$ denotes the Frobenius norm of the argument.

On the other hand, reference [58] uses a more complex connected auto-encoder mechanism for the X-ray image separation task. Various encoders and decoders are connected together to reconstruct the mixed X-ray image patch as well as RGB image patches of the front and rear sides, and a composite loss, containing reconstruction loss, energy loss

[1] This optimization problem was solved using a method based on a recursive decomposition of the mixed X-ray and visible images into low- and high-pass bands [55].

and dis-correlation loss, then was used as the loss function to learn the auto-encoders. These two approaches have led to substantially better separation results compared to [55], [57]. However, these approaches also exhibit some limitations:

- The method in [56] does not impose many constraints on the structure of x_1 and x_2, so it can also lead to separated individual X-ray images that share features with the corresponding individual RGB ones.
- The method in [58] in contrast imposes additional constraints on the various images, hence it leads to much better separation results. However, since the approach reported in [58] is largely heuristic, it is difficult to appreciate the reason a connected auto-encoder structure can lead to such remarkable mixed X-ray separation results.

Given the above limitations of the existing approaches, it's of huge significance to further improve the performance of X-ray image separation with side information. In this paper, we make our effort to proposed a deep learning approach for the X-ray image separation problem.

III. Proposed Approach

We deal with these limitations by proposing a new approach to separate mixed X-ray images taken from double-sided paintings given access to visible images on the front and rear part of the painting.

Our proposed approach is principled: it builds upon state-of-the-art sparsity-driven image processing techniques as well as sparsity-driven image separation with side information (akin to [55]), and it exploits algorithm unrolling techniques [59]. Interestingly, by using these various ideas, our approach also leads to a connected auto-encoder structure that is akin to the connected auto-encoder adopted in [58].

A. General structure

Suppose $x \in \mathbb{R}^{n_1 \times n_2}$ represents the mixed X-ray image patch, $x_1 \in \mathbb{R}^{n_1 \times n_2}$ and $x_2 \in \mathbb{R}^{n_1 \times n_2}$ represent the individual X-ray image patches, $r_{1,i} \in \mathbb{R}^{n_1 \times n_2}$ for $i = 1, 2, 3$ denotes the red, green and blue channel patches of one of the RGB images, and $r_{2,i} \in \mathbb{R}^{n_1 \times n_2}$ for $i = 1, 2, 3$ denote the red, green and blue channel patches of the other RGB image.

The general structure of the proposed connected auto-encoder is depicted in Fig. 2, where $\hat{x}$ is the reconstructed mixed X-ray, $\hat{r}_{1,i}$ and $\hat{r}_{2,i}$ denote the regenerated RGB image of the front and rear painting of the ith channel, respectively, $z_1^k \in \mathbb{R}^{n_1 \times n_2}$ and $z_2^k \in \mathbb{R}^{n_1 \times n_2}$ denote the sparse representations underlying the image patches on the front and rear sides of the painting, respectively, and $k = 1, 2, \cdots, K$ indexes the channel number. n_1 and n_2 denote the number of pixels for each image patch with respect to horizontal and vertical directions, respectively. Note that as we propose a convolutional model, which will be illustrated in the following subsection, both sparse codes z_1 and z_2 have K channels in total.

Our connected auto-encoder consists of various components:

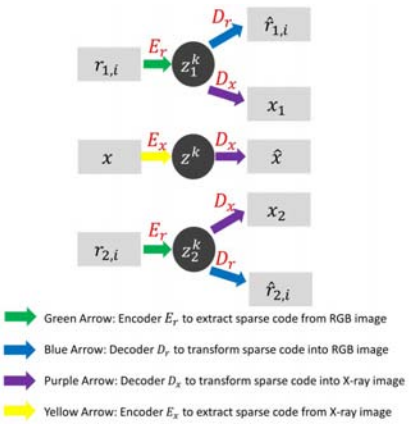

Fig. 2. General structure of the connected auto-encoder.

- Encoder E_r (represented by the green arrows) is used to extract sparse features z_1 and z_2 from the RGB image patches r_1 and r_2, respectively. This is done by adopting the feed-forward neural network structures derived later.
- Encoder E_x (represented by the yellow arrows) is used to extract sparse feature z from the mixed X-ray image patches x. This is also done by adopting the feed-forward neural network structure derived later.
- Decoder D_r (represented by the blue arrows) is used to convert the sparse features z_1 and z_2 into an estimate of the RGB image patches $\hat{r}_1$ and $\hat{r}_2$, respectively.
- Decoder D_x (represented by the purple arrow) is also used to convert the features z into an estimate of the X-ray image patches x.

The connection between the auto-encoders lies in two aspects: 1) they share the same encoders and decoders, i.e., E_r, E_x, D_r, and D_x, and 2) the various auto-encoders will be learnt together by leveraging a joint loss.

In the following subsection, we design the various encoders using the algorithm unrolling technique and the decoders based on a convolutional sparse coding model.

B. Model

The progressive attenuation of an X-ray beam as it passes through matter can be denoted by the Beer-Lambert Law [1], [62], [63] as follows

$$I = I_0 e^{-\alpha h t} \tag{8}$$

where h denotes the density of the material, t denotes the thickness of material, α_1 denotes the attenuation coefficient, and I_0 is the intensity of the initial beam.

Based on traditional film-based X-radiography, in regions where more X-rays go through the material (i.e. less attenuation) the resulting X-ray image appears dark, whereas in regions where fewer X-rays penetrate through the material (i.e. more attenuation) the image appears lighter. Supposing that the X-ray images are normalized, i.e., the value at each pixel of the X-ray images vary between 0 and 1, this will mean that the X-ray intensity measured has decayed fully in areas with the value 1. Thus, 1 minus the value of the X-ray image would describe the remaining X-ray intensity after

going through the material. Then, the mixed X-ray image patch x can be expressed in terms of the individual X-ray image patches x_1 and x_2 as follows:

$$\begin{aligned} 1-x_1 &= I_1 = I_0 e^{-\alpha_1 h_1 t_1} \\ 1-x_2 &= I_2 = I_0 e^{-\alpha_2 h_2 t_2} \\ 1-x &= I = I_0 e^{-\alpha_1 h_1 t_1 - \alpha_2 h_2 t_2} \end{aligned} \tag{9}$$

where h_1 and h_2 denote the density of the material for both sides of the painting, t_1 and t_2 denote the thickness of material for both sides, and α_1 and α_2 denote the attenuation coefficients for both sides. In this model, it is assumed that the attenuation from the support material that the X-rays pass through is minor and so is not included and h, t and α values relate to the two paint layers (one on front and one on back of support). So then we are talking about the two painted sides only

According to (9), we have

$$\log(1-x) = \log(1-x_1) + \log(1-x_2). \tag{10}$$

Then, there exists one constraint between the mixed X-ray image and separated individual X-ray images as follows:

$$1-x = (1-x_1)(1-x_2). \tag{11}$$

During the training phase of the proposed approach, we will add one regularization term to guarantee this constraint.

We propose to use convolutional sparse coding techniques to model each individual image patch. The convolutional sparse coding paradigm is an extension of the sparse coding model, in which a redundant dictionary is modeled as a concatenation of circulant matrices. While the global sparsity constraint describes the target signal as a linear combination of a few atoms in the redundant dictionary.

We adopt this model because it has been shown to lead to state-of-the-art performance in various image processing tasks [60]. It can also be coupled with algorithm unrolling techniques to lead to convolutional neural networks [61]. The convolutional sparse coding model is shown as follows:

$$\begin{aligned} r_{1,i} &= \sum_{k=1}^{K} \Phi_i^k * z_1^k, \quad r_{2,i} = \sum_{k=1}^{K} \Phi_i^k * z_2^k, \\ x_1 &= \sum_{k=1}^{K} \Theta^k * z_1^k, \quad x_2 = \sum_{k=1}^{K} \Theta^k * z_2^k, \\ x &= \sum_{k=1}^{K} \Theta^k * z^k, \end{aligned} \tag{12}$$

where $\Phi_i^k \in \mathbb{R}^{M \times M}$ denotes the k-th convolutional dictionary filter for the RGB image patches of the ith channel, $\Theta^k \in \mathbb{R}^{M \times M}$ denotes the k-th convolutional dictionary filter for the X-ray image patches, and $*$ denotes the convolution processing. The convolution operation $c = a * b$ between two image patches a and b is given by:

$$c(i,j) = \sum_p \sum_q a(p,q) b(i-p+1, j-q+1). \tag{13}$$

Note that this model immediately links the various images by imposing that the X-ray and RGB image patches associated with the same side of the painting share the same sparse representation. This model also imposes that the mixed X-ray image is equal to the sum of the individual X-ray images (as in other works mentioned earlier) since $1-x = (1-x_1)(1-x_2)$.

C. Connected auto-encoder details

We now show the details of the design of the various encoders and decoders.

Firstly, we propose to separate the mixed X-ray image patch into its individual constituent image patches given access to the individual RGB image patches by using a connected auto-encoder structure derived from a sparsity-driven optimization problem akin to that in (4). In particular, if we have access to the dictionaries Θ_k and Φ^k, for $k = 1, \ldots, K$, we can recover the underlying sparse representations by adopting the following optimization problem:

$$\begin{aligned} \min_{z^k, z_1^k, z_2^k} \quad & \|x - \sum_{k=1}^{K} \Theta^k * z^k\|_F^2 + \lambda \sum_{k=1}^{K} \|z^k\|_1 \\ & + \sum_{i=1}^{3} \|r_{1,i} - \sum_{k=1}^{K} \Phi_i^k * z_1^k\|_F^2 + \lambda \sum_{k=1}^{K} \|z_1^k\|_1 \\ & + \sum_{i=1}^{3} \|r_{2,i} - \sum_{k=1}^{K} \Phi_i^k * z_2^k\|_F^2 + \lambda \sum_{k=1}^{K} \|z_2^k\|_1 \\ \text{s.t.} \quad & 1-x = (1 - \sum_{k=1}^{K} \Theta^k * z_1^k)(1 - \sum_{k=1}^{K} \Theta^k * z_2^k). \end{aligned} \tag{14}$$

where λ is the regularization parameter. One can then also recover the individual X-ray images based on (12).

We can now turn this optimization problem into a connected auto-encoder by following a four step procedure:

1) Firstly, we decouple the original optimization problem into three separate optimization problems.
2) Secondly, we develop solvers to each such individual optimization problem using convolutional iterative thresholding (CISTA) algorithms.
3) Thirdly, we turn such CISTA solvers into a layered network architecture – denoted by CLISTA – using algorithm unrolling techniques.
4) Finally, we recouple the various individual networks into an overall network, leading up to a connected auto-encoder structure whose parameters can be further learnt in a totally self-supervised manner under a joint loss function that couples the various constituent networks.

We acknowledge that there may not be guarantees that this decoupling and recoupling strategy leads to a solution that coincides to that of the original problem in (13). However, numerical results demonstrate outstanding performance.

We describe these steps further below.

1) Decoupling: Our first step is to decouple the original optimization problem in (13) into three individual optimization

problems given by:

$$\begin{aligned}
&\min_{z^k} \quad \|x - \sum_{k=1}^{K} \Theta^k * z^k\|_F^2 + \lambda \sum_{k=1}^{K} \|z^k\|_1 \\
&\min_{z_1^k} \quad \sum_{i=1}^{3} \|r_{1,i} - \sum_{k=1}^{K} \Phi_i^k * z_1^k\|_F^2 + \lambda \sum_{k=1}^{K} \|z_1^k\|_1 \\
&\min_{z_2^k} \quad \sum_{i=1}^{3} \|r_{2,i} - \sum_{k=1}^{K} \Phi_i^k * z_2^k\|_F^2 + \lambda \sum_{k=1}^{K} \|z_2^k\|_1, \qquad (15)
\end{aligned}$$

Again, it is clear that the solutions to the optimization problems in (15) do not have to coincide with the solutions to the optimization problems in (14) in view of the fact that we are explicitly dropping the constraint $1 - x = (1 - x_1)(1 - x_2)$. We will deal with this constraint *a posteriori* in step 4 (see section III.D).

2) Solver: Our second step is to develop an iterative solver for each individual optimization problem appearing in (15). Let us first consider the optimization problem given by:

$$\min_{z^k} \quad \|x - \sum_{k=1}^{K} \Theta^k * z^k\|_F^2 + \lambda \sum_{k=1}^{K} \|z^k\|_1. \qquad (16)$$

A solution to this optimization problem can be computed iteratively by adopting a convolutional iterative soft thresholding algorithm (CISTA) as follows:

$$z^{k,j} = \mathcal{S}_{\frac{\lambda}{L}} \left(z^{k,j-1} + \frac{1}{L} (\Theta^k)^T * (x - \sum_{m=1}^{K} \Theta^m * z^{m,j-1}) \right), \qquad (17)$$

where $z^{k,j}$ denotes the sparse representation associated with the kth filter at iteration j, $(\Theta^k)^T$ denotes the transpose of Θ^k, $L > 0$ is the step size and operator $S_{\frac{\lambda}{L}}(\cdot)$ is the soft thresholding operator, and is applied element-wise on its vector argument as follow:

$$\mathcal{S}_{\frac{\lambda}{L}}\{x\} = \text{sign}(x) \cdot \max(|x| - \frac{\lambda}{L}, 0). \qquad (18)$$

Equation (17) can also be rewritten as:

$$z^j = \mathcal{S}_{\frac{\lambda}{L}} \left(z^{j-1} + \frac{1}{L} \Theta^T \star \left(x - \sum (\Theta \star z^{j-1}) \right) \right) \qquad (19)$$

where $z^j = [z^{1,j}, z^{2,j}, \cdots, z^{K,j}] \in \mathbb{R}^{n_1 \times n_2 \times K}$ denote the series of sparse representations associated with the different filters at iteration j, $\Theta = [\Theta^1, \Theta^2, \cdots, \Theta^K] \in \mathbb{R}^{M \times M \times K}$ is an array of K $M \times M$ filters, $\Theta^T = [(\Theta^1)^T, (\Theta^2)^T, \cdots, (\Theta^K)^T] \in \mathbb{R}^{M \times M \times K}$ is the transposed version of Θ, and $\sum$ denotes the summation along the third dimension. Symbol $\star$ denotes the convolution along the first and second dimension, i.e.,

$$\begin{aligned}
&\Theta \star z^j = [\Theta^1 * z^{1,j}, \Theta^2 * z^{2,j}, \cdots, \Theta^K * z^{K,j}] \\
&\Theta \star x = [\Theta^1 * x, \Theta^2 * x, \cdots, \Theta^K * x]. \qquad (20)
\end{aligned}$$

Similarly, a solution to the optimization problems given by:

$$\begin{aligned}
&\min_{z_1^k} \quad \sum_{i=1}^{3} \|r_{1,i} - \sum_{k=1}^{K} \Phi_i^k * z_1^k\|_F^2 + \lambda \sum_{k=1}^{K} \|z_1^k\|_1 \\
&\min_{z_2^k} \quad \sum_{i=1}^{3} \|r_{2,i} - \sum_{k=1}^{K} \Phi_i^k * z_2^k\|_F^2 + \lambda \sum_{k=1}^{K} \|z_2^k\|_1, \qquad (21)
\end{aligned}$$

can also be computed iteratively using CISTA as follows:

$$\begin{aligned}
&z_1^{k,j} = \\
&\mathcal{S}_{\frac{\lambda}{L}} \left(z_1^{k,j-1} + \sum_{i=1}^{3} \left(\frac{1}{L} (\Phi_i^k)^T * (r_{1,i}^k - \sum_{m=1}^{K} \Phi_i^m * z_1^{m,j-1}) \right) \right), \\
&z_2^{k,j} = \\
&\mathcal{S}_{\frac{\lambda}{L}} \left(z_2^{k,j-1} + \sum_{i=1}^{3} \left(\frac{1}{L} (\Phi_i^k)^T * (r_{2,i}^k - \sum_{m=1}^{K} \Phi_i^m * z_2^{m,j-1}) \right) \right), \qquad (22)
\end{aligned}$$

where $z_1^{k,j}$ and $z_2^{k,j}$ denote sparse representations associated with the kth filter at iteration$j$ for the front and rear paintings, respectively. (22) can also be rewritten as:

$$\begin{aligned}
z_1^j &= \mathcal{S}_{\frac{\lambda}{L}} \left(z_1^{j-1} + \sum_{i=1}^{3} \left(\frac{1}{L} \Phi_i^T \star \left(r_{1,i} - \sum (\Phi_i \star z_1^{j-1}) \right) \right) \right) \\
z_2^j &= \mathcal{S}_{\frac{\lambda}{L}} \left(z_2^{j-1} + \sum_{i=1}^{3} \left(\frac{1}{L} \Phi_i^T \star \left(r_{2,i} - \sum (\Phi_i \star z_2^{j-1}) \right) \right) \right), \qquad (23)
\end{aligned}$$

where $z_1^j = [z_1^{1,j}, z_1^{2,j}, \cdots, z_1^{K,j}]$, $z_2^j = [z_2^{1,j}, z_2^{2,j}, \cdots, z_2^{K,j}]$ and $\Phi_i = [\Phi_i^1, \Phi_i^2, \cdots, \Phi_i^K] \in \mathbb{R}^{M \times M \times K}$.

3) Unfolding: Our third step is to convert the iterative solver into a feedforward layered neural network architecture using unfolding techniques [59]. In particular, we re-write (19) as follows

$$z^j = \mathcal{S}_\epsilon \left(z^{j-1} + W_{\Theta 2} \star \left(x - \sum (W_{\Theta 1} \star z^{j-1}) \right) \right), \qquad (24)$$

where we have replaced the original parameters Θ, $\frac{1}{L}\Theta^T$, $\frac{\lambda}{L}$ using new parameters $W_{\Theta 1}$, $W_{\Theta 2}$ and ϵ. We can then map each solver iteration operation into a feedforward neural network operation; and likewise we can also map J solver iterations into a J layer feedforward neural network. Each network layer is represented in Fig. 3.

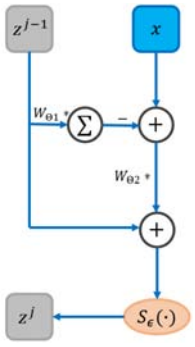

Fig. 3. Layer structure associated with (24).

Likewise, we can also rewrite (23) as follows:

$$z_1^j = \mathcal{S}_\epsilon\left(z_1^{j-1} + \sum_{i=1}^{3}\left(W_{\Phi 2,i} \star \left(r_{1,i} - \sum(W_{\Phi 1,i} \star z_1^{j-1})\right)\right)\right)$$
$$z_2^j = \mathcal{S}_\epsilon\left(z_2^{j-1} + \sum_{i=1}^{3}\left(W_{\Phi 2,i} \star \left(r_{2,i} - \sum(W_{\Phi 1,i} \star z_2^{j-1})\right)\right)\right), \tag{25}$$

where we have also replaced the original parameters Φ_i, $\frac{1}{L}\Phi_i^T$, $\frac{\lambda}{L}$ by parameters $W_{\Phi 1,i}$, $W_{\Phi 2,i}$ and ϵ. This then also maps J iterations of the algorithm into a J layer feedforward neural network with each layer depicted in Fig. 4.

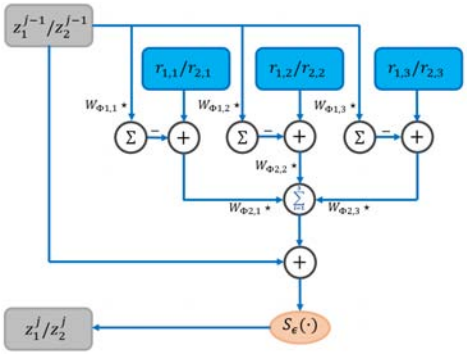

Fig. 4. Layer structure associated with (25).

The rationale for adopting new parameters to describe the neural network layer instead of the original ones derives from the fact that we can further learn this using entirely self-supervised mechanisms, as described next in Step 4.

Note that the learnable parameters $W_{\Theta 1}$, $W_{\Theta 2}$, $W_{\Phi 1,i}$, $W_{\Phi 2,i}$ and ϵ are set to vary in each layer to give the proposed network more freedom to achieve better separation performance.

4) Recoupling: Finally, we assemble the various individual convolutional neural networks that attempt to solve the optimization problems appearing in (14) into a connected auto-encoder structure that attempts to solve the original optimization problem appearing in (15). The general structure of the proposed connected auto-encoder is shown in Fig. 2.

Decoder D_r is designed as

$$\hat{r}_{1,i} = \sum(W_{\Phi,i} \star z_1)$$
$$\hat{r}_{2,i} = \sum(W_{\Phi,i} \star z_2), \tag{26}$$

where $W_{\Phi,i} \in \mathbb{R}^{M\times M\times k}$ denotes a convolutional layer, $z_1 = z_1^J$ and $z_2 = z_2^J$ denote the sparse codes of the front and rear image patch, respectively, and J layers are assumed to be used in the encoder E_r.

In a similar manner, decoder D_x is designed as follows:

$$\hat{x} = \sum(W_\Theta \star z) \tag{27}$$

where $W_\Theta \in \mathbb{R}^{M\times M\times k}$ denotes a convolutional layer and $z = z^J$ denotes the sparse code of the mixed X-ray image patch, and J layers are assumed to be used in the encoder E_x.

Our connected auto-encoder is also such that the encoders associated with the RGB images are equal (i.e. they share the same weights) but the encoder associated with the mixed X-ray image is different; likewise, the decoders associated the two RGB images share the same convolutional layer. Note the reason we use decoders to map the underlying sparse representations to estimates of the original mixed X-ray image and the original RGB images is to allow learning the connected auto-encoder parameters in a totally self-supervised manner.

D. Training strategy

Finally, in view of the fact that the parameters of the various encoders and decoders in our auto-encoder structure are learnable, we propose to tune these parameters by using the loss function given by:

$$\begin{aligned}\min_W \quad & \frac{1}{S}\sum_{s=1}^{S}\sum_{i=1}^{3}\|r_{1,i}^s - \hat{r}_{1,i}^s\|_F^2 + \|r_{2,i}^s - \hat{r}_{2,i}^s\|_F^2 \\ & + \frac{1}{S}\sum_{s=1}^{S}\|x^s - \hat{x}^s\|_2^2 \\ & + \frac{1}{S}\sum_{s=1}^{S}\lambda\|z^s\|_1 + \lambda\|z_1^s\|_1 + \lambda\|z_2^s\|_1 \\ & + \frac{1}{S}\sum_{s=1}^{S}\mu\|1 - x^s - (1-x_1^s)(1-x_2^s)\|_2^2. \end{aligned} \tag{28}$$

where $W = \{W_{\Theta 1}, W_{\Theta 2}, W_\Theta, W_{\Phi 1,i}, W_{\Phi 2,i}, W_{\Phi,i}, \epsilon\}$ denote the weights of the connected auto-encoder, superscript s is the patch-wise index and it is assumed that we have S patches in total.

This loss consists of various components:

1) The first and second components make sure the connected auto-encoder maps patches of the RGB images to themselves;
2) The third component makes sure the connected auto-encoder also maps patches of the mixed X-ray image to itself;
3) The remaining three components attempt to promote sparsity of the underlying sparse representations;
4) The fi nal component attempts to enforce the constraint $(1-x) = (1-x_1)(1-x_2)$ in (14), thereby connecting the various sparse representations.

The regularization parameters λ and μ trade-off the effect of these various overall loss components. We use the set of regularization parameters $\lambda = 10^{-4}$ and $\mu = 3$. The method used to select the regularization parameters λ and μ is shown in section IV-B.

We then optimize the learnable parameters by using stochastic gradient descent (SGD) with constant learning rate 0.00001. We set $J = 5$, i.e., we have 5 layers in the encoders E_x and E_r, $M = 5$ and $K = 64$.

E. Approach comparison

While the proposed approach is similar to [57], there are a number of differences and these differences include

- **Model:** We formulate the mixture model of the X-ray image based on the physically more meaningful attenuation model, and correspondingly, the addition mixture model in [58] that $x \approx x_1 + x_2$ is changed into $1 - x = (1 - x_1)(1 - x_2)$ in this paper. The novel mixture model gives the hypothesis of the proposed approach rationality and theoretical basis. We also formulated the X-ray image separation problem with side information into a convolutional sparse coding model, while the approach reported in [58] is more heuristic. Comparatively, the proposed algorithm gives a more intuitive explanation of the X-ray image separation problem from the perspective of mathematical modeling.
- **Structure:** In the proposed algorithm, the encoders are designed based on unrolling the sparse coding algorithm into a neural network architecture, and decoders are designed based on the linear sparse coding model shown in (10), while the network structure in [58] is designed empirically by using different convolutional neural networks in both encoder and decoder.
- **Loss:** In the proposed algorithm, we added an l_1 norm constraint on the sparse feature maps and another loss to minimize the difference between the sparse feature maps of the mixed X-ray image and sum of separated X-ray images, and in addition, we deleted the energy loss and dis-correlation loss adopted in [58] as they were no longer required (see the results section of the paper).

IV. Experimental Results

We conducted a number of experiments to assess the effectiveness of our proposed X-ray image separation approach. These involved:

- an analysis of the effect of the various regularization parameters associated with our approach on X-ray image separation performance;
- an analysis of the effectiveness of our approach in relation to the state-of-the-art, both on synthetically mixed X-ray images and real mixed X-ray images (the results on synthetically mixed X-ray data are shown in the supplementary material).

The effectiveness of our approach is reported both quantitatively and qualitatively. For a qualitative assessment of the separation performance of our approach, we report a number of performance metrics. Of particular reference, Peak Signal to Noise Ratio (PSNR), average Structural Similarity (SSIM), average Interference to Signal Ratio (ISR) [64], and average normalized correlation coefficients (NCC) [65], [66] are exploited to evaluate the separation performance.

A. Datasets

Our experiments rely on a number of datasets associated with real paintings, including:

- The *Ghent Altarpiece* by Hubert and Jan van Eyck. This large, complex 15th-century polyptych altarpiece comprises a series of panels – including panels with a composition on both sides (see Fig. 1) – that we use to showcase the performance of our algorithm on real mixed X-ray data.
- *Lady Elizabeth Thimbelby and Dorothy, Viscountess Andover* by Anthony van Dyck (Fig. 5). This one-sided canvas painting was used to design a number of experiments allowing us to understand the impact of the various regularization parameters associated with our separation approach.

B. Regularization Parameter Selection Protocol

In this section, we present experiments to assess the effectiveness of our proposed X-ray image separation approach. These involved an analysis of the effect of the various regularization parameters associated with our approach on X-ray image separation performance. Our experiments used the dataset associated Anthony van Dyck's painting of Lady Elizabeth Thimbelby and Dorothy, Viscountess Andover (Fig. 5). This canvas painting is painted on one side and was used to design a number of experiments allowing us to understand the impact of the various regularization parameters associated with our separation approach.

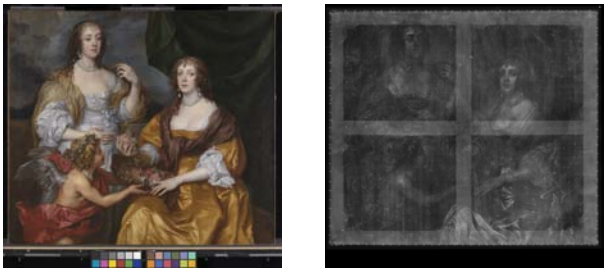

(a) (b)

Fig. 5. Anthony van Dyck, *Lady Elizabeth Thimbelby and Dorothy, Viscountess Andover* (NG6437), about 1635. Oil on canvas © The National Gallery, London. (a). RGB image. (b). X-ray image.

1) Experimental set-up: We use two small areas with the same size from the oil painting *Lady Elizabeth Thimbelby and Dorothy, Viscountess Andover* by Anthony van Dyck, one associated with the face of Lady Elizabeth Thimbelby and the other with the face of her sister in the portrait, in order to create a synthetically mixed X-ray image. The corresponding RGB images, X-ray images, and synthetically mixed X-ray image are shown in Fig. 6. The synthetically mixed X-ray image in Fig. 6 (e) is obtained by mixing the X-ray images shown in Fig. 6 (c) and Fig. 6 (d) based on the model shown in (11).

Each such image is of size 1100×1100 pixels. These images were then further divided into patches of size 64×64 pixels with 56 pixels overlap (both in the horizontal and vertical direction), resulting in 11,236 patches. Each patch associated with the synthetically mixed X-ray image was separated independently; the various patches associated with the individual separated X-ray images are then put together by placing various patches in the original order and averaging the overlapping portions.

We carried out the separation experiments over a number of trials associated with different random initializations of the auto-encoders in our method. We then assessed the separation

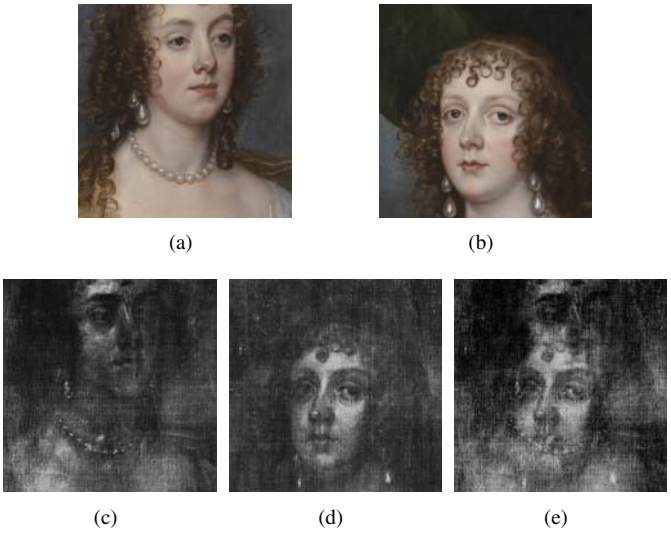

(a) (b) (c) (d) (e)

Fig. 6. Images used for regularization parameter selection (small areas of *Lady Elizabeth Thimbelby and Dorothy, Viscountess Andover* shown in Fig. 5). (a). First RGB image. (b). Second RGB image. (c). X-ray image corresponding to first RGB image. (d). X-ray image corresponding to second RGB image. (e). Synthetically mixed X-ray image.

performance by reporting on the average PSNR, SSIM, ISR and NCC.

This experimental procedure was carried out for different combinations of regularization parameters λ and μ appearing in (24) of the main manuscript. We restricted these regularization parameters to lie in the interval $\log_{10}\lambda \in [-5, 0]$ and $\mu \in [0, 6]$, we also selected instances of the regularization parameters from this interval in steps of 0.1 and 0.02, respectively.

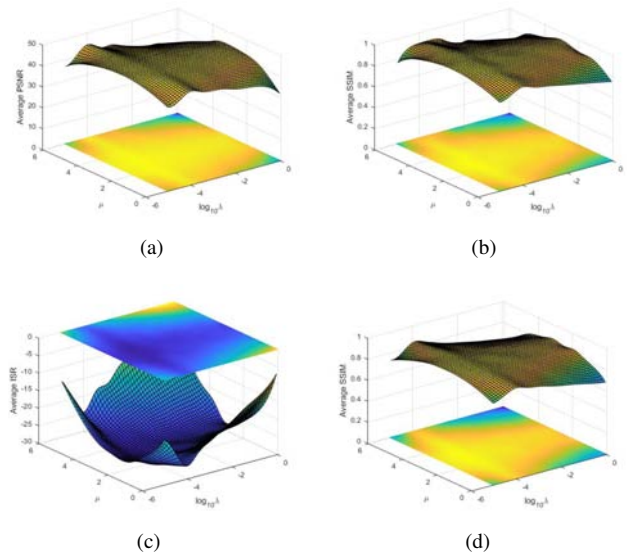

(a) (b) (c) (d)

Fig. 7. Quantitative metrics as functions of λ and μ. (a). Average PSNR. (b). Average SSIM. (c). Average ISR. (d). Average NCC.

2) Effect of regularization parameters λ and μ: Fig. 7 depicts the average PSNR, SSIM, ISR and NCC as functions of the regularization parameters λ and μ. It is clear that different regularization parameter values result in different separation performances. For example,

- Fig. 7 suggests that the regularization parameter values leading to the best quantitative metrics performance are $\lambda = 10^{-4}$ and $\mu = 3$. Fig. 8 (a) and (b) also confirm that the separated X-ray images are very similar to their ground truth counterparts.
- With $\lambda = 10^{-5}$, $\mu = 0$, the loss function component

$$L_r = L_{r1} + L_{r2} \tag{29}$$

dominates over other components, implying one tends to promote fidelity of the reconstruction of the individual RGB images and the mixed X-ray image, where

$$L_{r1} = \frac{1}{S}\sum_{s=1}^{S}\sum_{i=1}^{3} \|r_{1,i}^s - \hat{r}_{1,i}^s\|_F^2 + \|r_{2,i}^s - \hat{r}_{2,i}^s\|_F^2$$
$$L_{r2} = \frac{1}{S}\sum_{s=1}^{S} \|x^s - \hat{x}^s\|_2^2. \tag{30}$$

Fig. 7 suggests that this may result in relatively worse quantitative metrics and Fig. 8 (c) and (d) also confirm that the separated X-ray images are very similar to the original mixed X-ray image.
- With $\lambda = 1$, $\mu = 0$, the loss function component

$$L_s = \frac{1}{S}\sum_{s=1}^{S} \lambda\|z^s\|_1 + \lambda\|z_1^s\|_1 + \lambda\|z_2^s\|_1 \tag{31}$$

dominates over other components, implying one tends to promote the sparsity of the feature maps. Fig. 7 suggests that this also results in relatively worse quantitive metrics and Fig. 8 (e) and (f) also confirm that the separated X-ray images are seriously blurred and very similar to the corresponding grayscale versions of the visible RGB images (thereby losing information present in X-ray images associated with sub-surface design features such as previous compositions and *pentimenti*, concealed areas of damage or structural features such as the wood grain (for paintings on panel) or canvas weave and wooden stretcher bars (for paintings on canvas).
- With $\lambda = 10^{-5}$, $\mu = 6$, the loss function component

$$L_c = \frac{1}{S}\sum_{s=1}^{S} \mu\|1 - x^s - (1 - x_1^s)(1 - x_2^s)\|_2^2 \tag{32}$$

dominates over other components, implying one tends to guarantee that sparse feature maps should meet the constraint $1 - x = (1 - x_1)(1 - x_2)$. Fig. 7 suggests that this may result in a relatively high average separation average MSE, low average PSNR and low average SSIM, and Fig. 8 (g) and (h) reveal that the separated X-ray image is seriously blurred, and contain some unwanted mutual information.

To summarize, based on these results, in our experiments reported in the main paper, we use the set of regularization parameters $\lambda = 10^{-4}$ and $\mu = 3$.

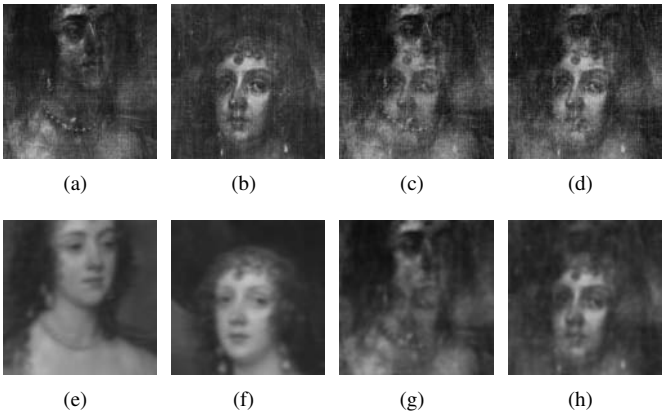

Fig. 8. X-ray separation results: (a) and (b) Separated X-ray images for $\lambda = 10^{-4}$ and $\mu = 3$; (c) and (d) Separated X-ray images for $\lambda = 10^{-5}$, $\mu = 0$; (e) and (f) Separated X-ray images for $\lambda = 1$, $\mu = 0$; (g) and (h) Separated X-ray images for $\lambda = 10^{-5}$, $\mu = 6$.

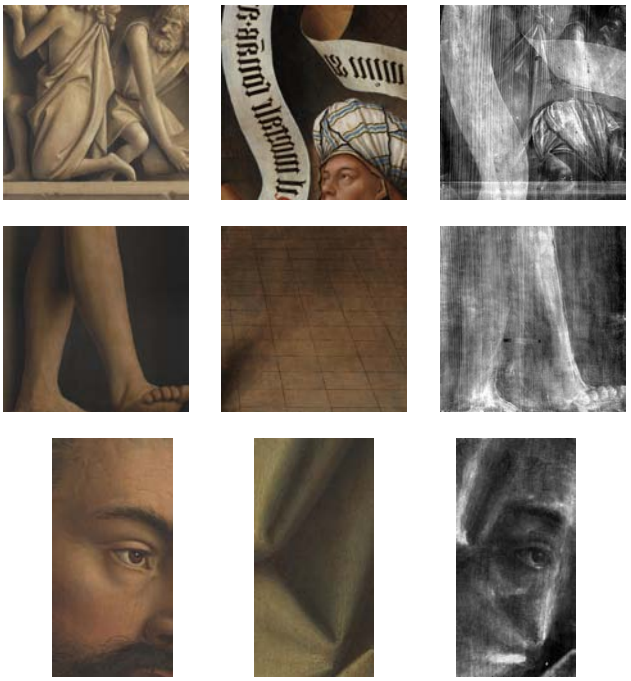

Fig. 9. Images used for real data experiments. Columns 1 to 3 correspond to the RGB image of the front side, the RGB image of the back of the panel (image reversed) and the mixed X-ray image, respectively. Rows 1 to 3 correspond to areas 1, 2, 3, respectively.

C. Experiments with Real Mixed X-ray Data

1) Set-up : In this experiment, we use three small areas from the *Ghent Altarpiece* (see Fig. 9). The first two areas are of size 1000×1000 pixels, while the third area is of size 600×1200 pixels.

The previous procedure was again followed: the two RGB images and the corresponding mixed X-ray image were divided into patches of size 64×64 pixels with 56 pixels overlap (both in the horizontal and vertical direction), resulting in 13,924 patches in the first two areas and 9,724 patches in the third area. The patches associated with the mixed X-ray image were separated independently. The various patches associated with the individual separated X-ray images were finally put together by placing various patches in the original order and averaging the overlap portions. All patches were also used in the training of the auto-encoders by randomly shuffling their order. Note that these three different areas are processed separately.

We adopted the regularization parameter values $\lambda = 10^{-4}$ and $\mu = 3$.

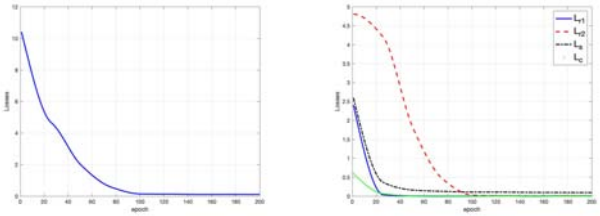

Fig. 10. Losses vs. number of epochs on area 1. (a). L_{total}. (b). L_{r1}, L_{r2}, L_s and L_c.

2) Results: Fig. 10 depicts the evolution of the overall loss function along with the individual ones as a function of the number of epochs on area 1. The observations in Fig. 10 depict that the total loss decreases gradually during the first 80 epochs. L_{r1}, L_s and L_c decrease dramatically in the first 25 epochs, and L_{r2} only decreases fast after epoch 25.

Fig. 11 depicts the evolution of the reconstruction of the various images as a function of the number of epochs on area 1. It is clear that the proposed algorithm has learnt how to reconstruct the RGB images by epoch 50; it is also clear that the algorithm only learns how to successfully reconstruct the individual X-ray images and the mixed one by epoch 100. Indeed, during the initial learning stages, the individual reconstructed X-ray images are very similar to grayscale versions of the RGB ones (e.g. the inscription on the banner that is present in the RGB images but should not be present in the X-ray images). By contrast, during the last learning stages, the individual reconstructed X-ray images become increasingly natural and contain much more detailed information.

Finally, Fig. 12 shows that the proposed algorithm produces much better separations than the algorithms in [56] and [58] on area 1. Specifically,

- Our algorithm – in contrast to that in [56] – also appears to reconstruct the pattern of cracking in the paint and the wood grain of the panel better, including more fine detail such as the crack on the right hand side of the reconstructed X-ray image for the front side.
- Our algorithm – again in contrast to that in [56] – also produces X-ray images without the addition of RGB image information not present in the true mixed X-ray image.
- The proposed algorithm produces two individual X-ray images that recombine almost perfectly to match the original mixed X-ray image. By contrast, the algorithms in [56] and [58] produce individual X-ray images that do not quite add up to the original mixed X-ray image, as the error maps of the reconstructed mixed X-ray images obtained by [56] and [58] than that achieved by the

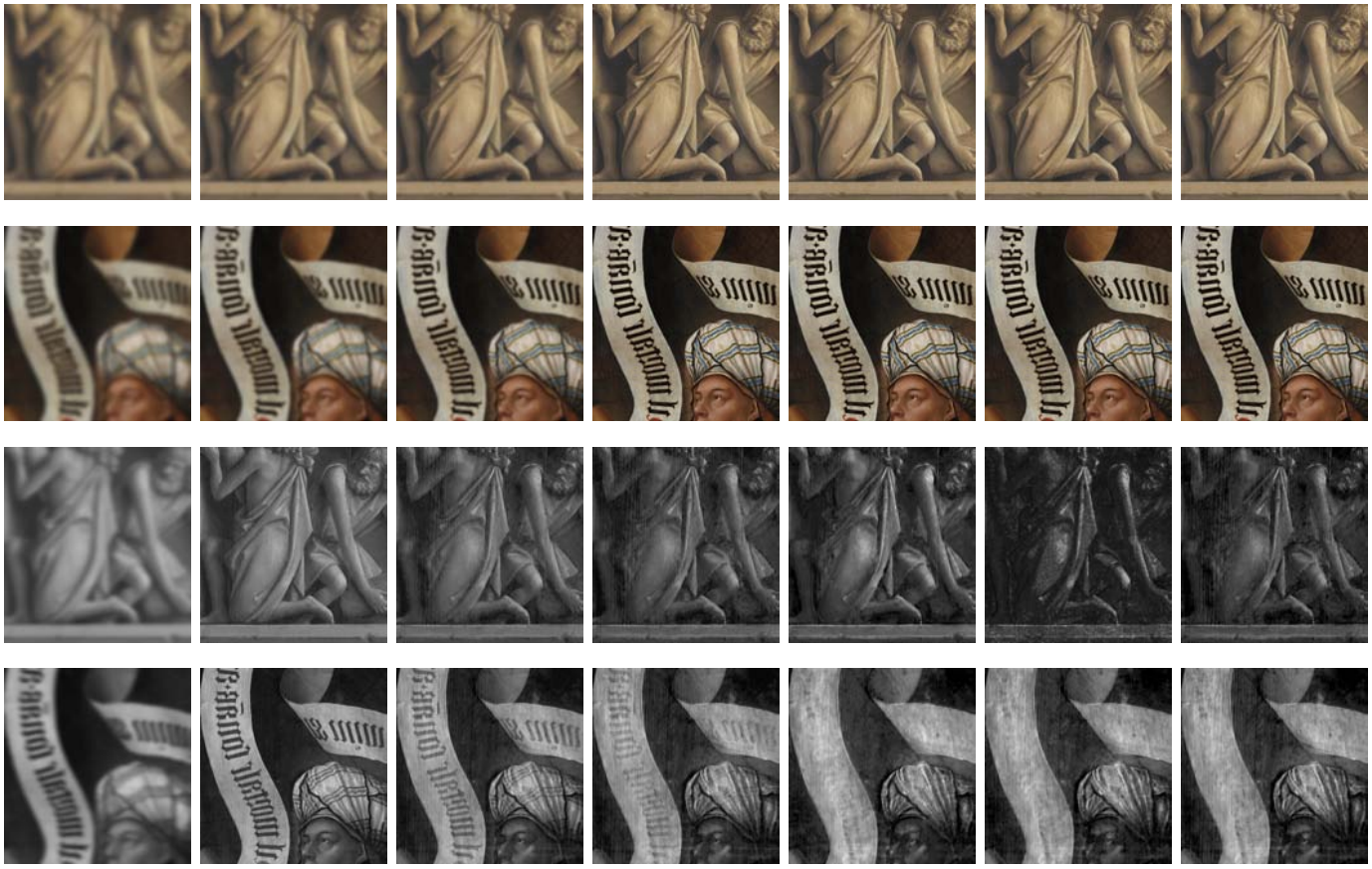

Fig. 11. Reconstructed images vs. number of epochs on area 1. Columns 1 to 7 correspond to reconstructed result after the 1st, 4th, 10th, 50th, 100th, 150th and 200th epoch, respectively. Rows 1 to 2 correspond to the reconstructed RGB images. Rows 3 to 4 correspond to the reconstructed X-ray images.

TABLE I
QUANTITATIVE ANALYSIS OF DIFFERENT APPROACHES

Methods	Metrics on the mixed X-ray images of area 1 (3rd column in Fig. 12)			
	average PSNR	average SSIM	average ISR	average NCC
[56]	18.1012	0.908	-26.35	0.827
[58]	32.4819	0.960	-41.59	0.927
Proposed approach	**39.6478**	**0.986**	**-49.57**	**0.988**
Methods	Metrics on the mixed X-ray images of area 2 (3rd column in Fig. 13)			
	average PSNR	average SSIM	average ISR	average NCC
[56]	17.5244	0.891	-30.51	0.852
[58]	37.5987	0.940	-45.62	0.931
Proposed approach	**45.8614**	**0.972**	**-52.64**	**0.979**
Methods	Metrics on the mixed X-ray images of area 3 (3rd column in Fig. 14)			
	average PSNR	average SSIM	average ISR	average NCC
[56]	18.4876	0.872	-25.34	0.894
[58]	36.6113	0.921	-41.38	0.944
Proposed approach	**41.0224**	**0.966**	**-47.49**	**0.982**

proposed approach. Note that – in contrast to the synthetic data experiments – it is not possible to compare the individual reconstructions to a ground truth.

The separation results using the different algorithms on area 2 and 3 are shown in Fig. 13 and Fig. 14, respectively. From the results, we can again observe that the proposed algorithm outperforms the methods in [56] and [58].

The corresponding quantitative metrics to evaluate the separation performance of the different approaches are given in Table I. Again, as with the visual comparisons in Fig. 13 and Fig. 14, the quantitative metrics, i.e., average PSNR, SSIM, ISR and NCC, demonstrate the superiority of the proposed algorithm. The reconstructed mixed X-ray images obtained using the proposed approach is closer to the ground truth than the approaches in [55] and [57]".

D. Ablation study

In this subsection, we utilize area 1 of the *Ghent Altarpiece* to conduct five ablation studies to verify the effectiveness of the proposed approach. The detailed information for each ablation study is noted in Table II. In studies I and II, we mainly verify the effectiveness of the proposed CLISTA network structure. Learnable iterative thresholding (LISTA) network architectures and CNN network architectures are exploited in studies I and II to replace the CLISTA network structure, respectively. In studies III, IV, and V, we focus on validating the effectiveness of the joint loss in (28), i.e., joint loss without loss function components L_r, L_s, and L_c are leveraged in studies III, IV and V, respectively.

The separation results of the different studies are shown in Fig. 15. In Fig. 15, rows 1 to 6 correspond to the results yielded by Study I, Study II, Study III, Study IV, Study V, and our proposed method, respectively. Columns 1 and 2 correspond to the reconstructed X-ray images, Columns

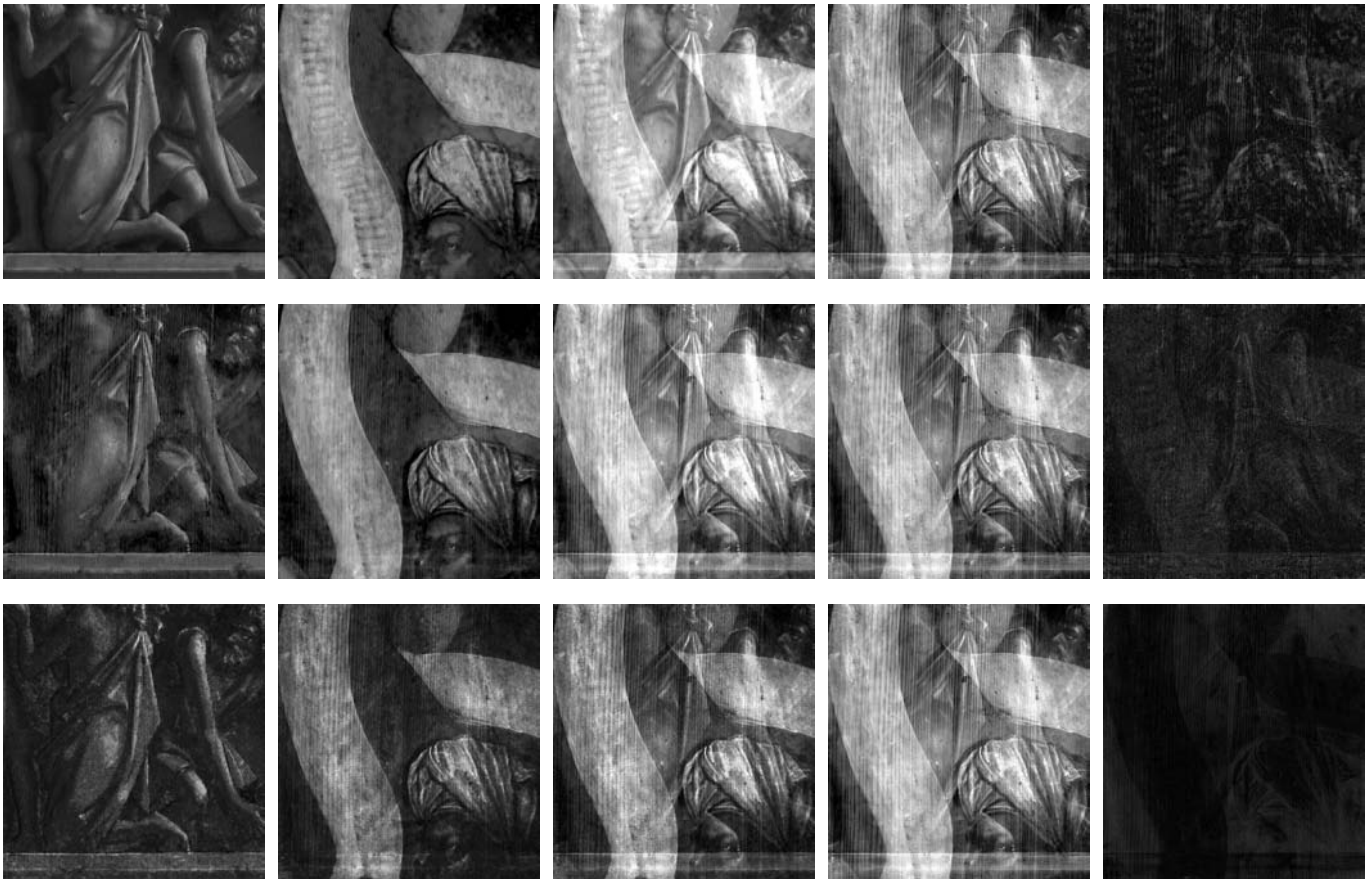

Fig. 12. Comparison of different X-ray separation methods on area 1. Rows 1 to 3 correspond to the results yielded by the method in [56], the method in [58] and our proposed method, respectively. Columns 1 and 2 correspond to the reconstructed X-ray images, Columns 3 and 4 correspond to the reconstructed and true mixed X-ray images, and Column 5 corresponds to the error maps.

TABLE II
DETAILED INFORMATION OF THE ABLATION STUDIES.

Studies	Detailed information
Study I	Using LISTA instead of CLISTA in the proposed approach
Study II	Using CNN instead of CLISTA in the proposed approach
Study III	Using joint loss without Loss function component L_r
Study IV	Using joint loss without Loss function component L_s
Study V	Using joint loss without Loss function component L_c

TABLE III
QUANTITATIVE ANALYSIS OF DIFFERENT ABLATION STUDIES

Methods	Metrics on the mixed X-ray images of area 1 (3rd column in Fig. 12)			
	average PSNR	average SSIM	average ISR(dB)	average NCC
Study I	35.8947	0.969	**-44.62**	**0.974**
Study Ii	30.9758	0.958	**-32.51**	**0.962**
Study III	32.1287	0.959	**-39.79**	**0.968**
Study IV	33.2318	0.965	**-42.17**	**0.970**
Study V	11.9549	0.827	**-22.68**	**0.879**
Proposed approach	**39.6478**	**0.986**	**-49.57**	**0.988**

3 and 4 correspond to the reconstructed and true mixed X-ray images, and Column 5 corresponds to the error maps. Comparing the last row in Fig. 12 with the first and second rows in Fig. 15, the effect of different network structures on the separation results using the proposed approach can be assessed and the CLISTA architecture can be seen to lead to a better performance than the LISTA and CNN architectures. The third row of Fig. 15 presents the separation results of the proposed approach without adopting reconstruction loss L_r. It can be seen that, without using the reconstruction loss L_r, the proposed approach fails to reconstruct high-quality separated individual X-ray images, as the first and second images in the third row of Fig. 15 contain information from both sides. The fourth row of Fig. 15 indicates that if the L_1 norm is not applied to constrain the sparse codes z_1, z_2 and z, the brightness of the separation result is high, resulting in a little distortion of the separated individual X-ray images. If the loss component L_c is not applied, the constraint $(1-x) = (1-x_1)(1-x_2)$ cannot be guaranteed, and correspondingly, the separated individual X-ray images are very similar to the corresponding grayscale versions of the RGB images.

The quantitative metrics, i.e., average PSNR, SSIM, ISR and NCC, used to evaluate the separation performance of the different ablation studies are given in Table III. Table III also indicates that the proposed approach described in the main text leads to better reconstructed mixed X-ray images than obtained in the different ablation studies.

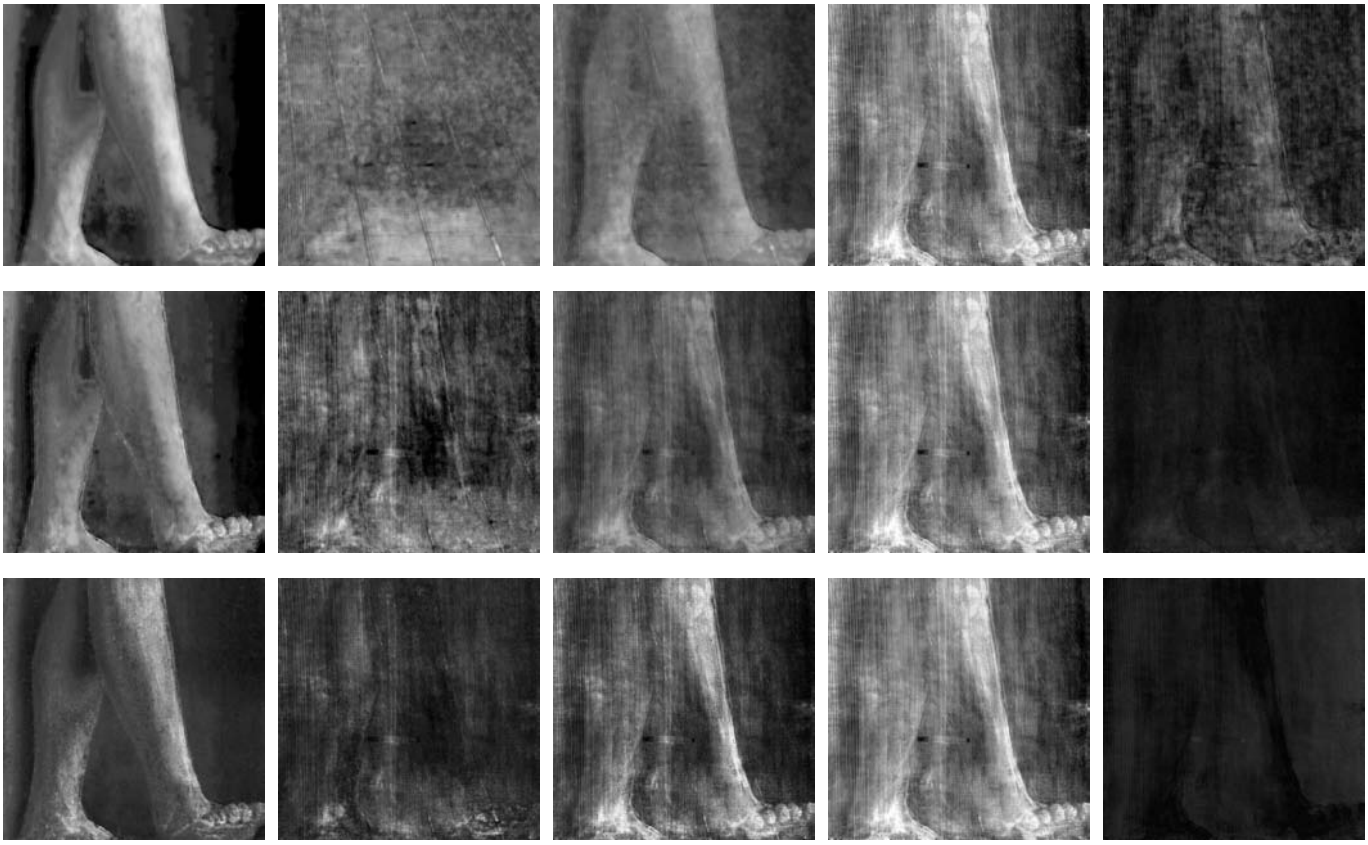

Fig. 13. Comparison of different X-ray separation methods on area 2. Rows 1 to 3 correspond to the results yielded by the method in [56], the method in [58] and our proposed method, respectively. Columns 1 and 2 correspond to the reconstructed X-ray images, Columns 3 and 4 correspond to the reconstructed and true mixed X-ray images, and Column 5 corresponds to the error maps.

E. Limitations

In this subsection, we discuss and present experiments to show the limitations of our proposed X-ray image separation approach. In our proposed approach, we assume that the mixed X-ray image is the mixture of the X-ray images of the two painted sides of the artwork and that these painted surfaces are the only attenuators on the incident X-ray intensity. However, if the assumption cannot be guaranteed, i.e., there is another layer or sub-surface detail with some additional content, the proposed approach is invalid, and it will be difficult to obtain well separated individual X-ray images for each painted side. Our model does not, for example, take account of the impact of the support material of a painting on the X-ray intensity. While generally attenuation from the support material will only be minor, in some instances the support may dominate the mixed X-ray image and our proposed appoach will no longer be valid. Even where the contribution of the support to the mixed X-ray image is small, if only two separated images are produced, how this contribution should be divided between the two separated X-ray images is unclear - both in terms of the mathematical model and to the heritage sector end user. As the separated X-ray images for the two paintings are hypothetical images there is no ground truth is available and for heritage sector end users, what it would be useful to be able to visualise (or to suppress) in the separated X-ray images may also depend on the particular painting or question being investigated.

Our approach has also not been tested on paintings where there is any degree of significant change within the painted layers that is not visible in the RGB images. For example, if there were changes within one or both paintings on a double-sided painting that had been completely concealed below subsequent layers of paint our approach might also struggle. It has also been assumed that the paint layers on both sides of a double-sided painting have similar properties (e.g. thickness, materials used etc) and if this is not the case issues may also be encountered. In such circumstances, the fact that X-ray images are collected from one side of a painting may impact on the results obtained as there will be more variation between the mixed X-rays obtained from different sides of the painting.

Experiments to demonstrate this phenomenon rely on the dataset associated with the painting *Lady Elizabeth Thimbelby and Dorothy, Viscountess Andover* by Anthony van Dyck (Fig. 5). In Fig. 5, the horizontal and vertical bars in the middle and around the painting are stretcher bars, structural elements of the support of the painting. We use two small areas from the painting with the same size, one area associated with the body of Lady Elizabeth Thimbelby and the other one with the body of her sister, in order to create a synthetically mixed X-ray image. Note that in both areas there are horizontal bars in the X-ray images. The horizontal bars are obvious with high energy, which will have a significant effect on our proposed approach. The corresponding RGB images, X-ray images, and

Fig. 14. Comparison of different X-ray separation methods on area 3. Rows 1 to 3 correspond to the results yielded by the method in [56], the method in [58] and our proposed method, respectively. Columns 1 and 2 correspond to the reconstructed X-ray images, Columns 3 and 4 correspond to the reconstructed and true mixed X-ray images, and Column 5 corresponds to the error maps.

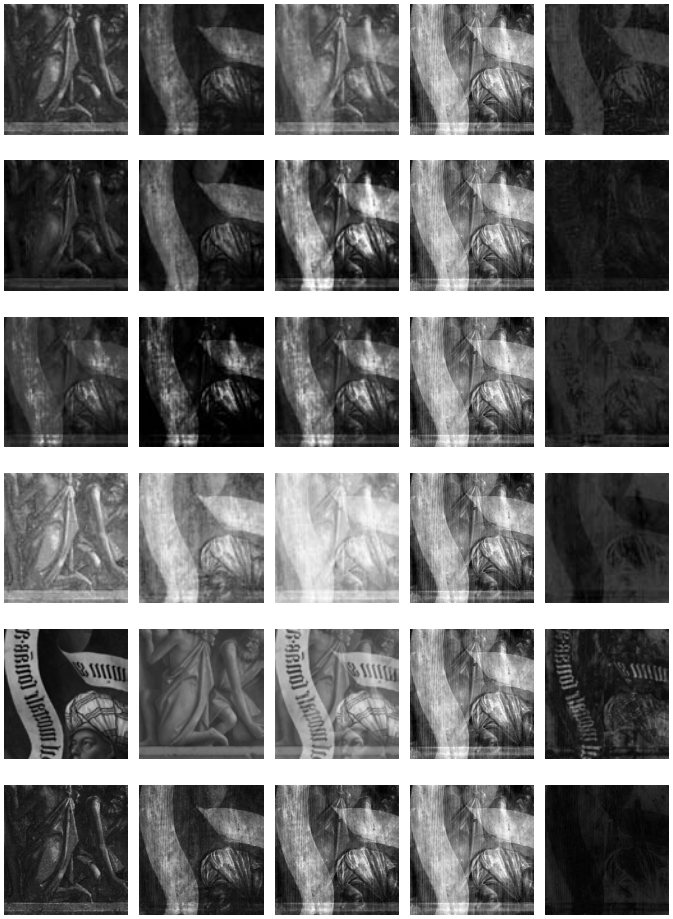

Fig. 15. Comparison of different ablation studies on area 1. Rows 1 to 6 correspond to the results yielded by Study I, Study II, Study III, Study IV, Study V, and our proposed method, respectively. Columns 1 and 2 correspond to the reconstructed X-ray images, Columns 3 and 4 correspond to the reconstructed and true mixed X-ray images, and Column 5 corresponds to the error maps.

synthetically mixed X-ray image are shown in Fig. 16. The synthetically mixed X-ray image in Fig. 16 (e) is obtained by mixing the X-ray images shown in Fig 16 (c) and Fig 16 (d) based on the model presented in (11).

The separation results of the proposed approach are shown in Fig. 17. These results suggest that the proposed approach cannot cope well with situations where the mixed X-ray image is dominated by additional content that does not relate to the painted design on either side of the artwork. However, it is able to correctly preserve details about paint thickness or brushstrokes etc captured in the mixed X-ray image where these relate to the painted designs. In addition, the horizontal stretcher bars that can be seen so clearly in the original individual X-ray images are not reconstructed successfully. Note that these limitations are also shared with other approaches.

V. Conclusion

X-ray images of polyptych wings, or other artworks painted on both sides of their support, contain in a single image content from both paintings, making them difficult for experts to interpret. It is therefore desirable to conceive approaches to separate the composite X-ray image into individual X-ray images containing content pertaining to one side only, in order to improve the utility of X-ray images in studying and conserving artworks.

This paper proposes a new approach to X-ray image separation. By leveraging sparsity-driven data models, sparsity-driven data processing, and algorithm unrolling techniques, we have derived a self-supervised learning approach based on the use of "connected" auto-encoders that extract sparse features from available side information, i.e. RGB images of the front and back of the artwork along with sparse features of the mixed X-ray image in order to reproduce both of the original RGB images and regenerate the mixed X-ray image. This approach allows image separation without the need for labelled data. A composite loss function is introduced to guide the training of the connected auto-encoders. On the basis of a number of quantitative metrics and qualitative visual assessment the approach outperforms the state-of-the-art separation algorithms, as verified by side-by-side experiments on images from a number of paintings. It should however be noted that with no absolute ground truth images available, assessing performance remains challenging and there are some details where the method in [57] possibly performs better. The model underlying the proposed method is however more physically meaningful than previous models, being based on

(a) (b) (c) (d) (e)

Fig. 16. Images used in the failure case (small areas of *Lady Elizabeth Thimbelby and Dorothy, Viscountess Andover* shown in Fig. 5). (a). First RGB image. (b). Second RGB image. (c). X-ray image corresponding to the first RGB image. (d). X-ray image corresponding to the second RGB image. (e). Synthetically mixed X-ray image.

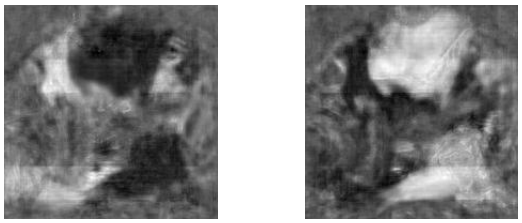

(a) (b)

Fig. 17. Separation results of the failure case. (a). First individual separated X-ray image. (b). Second individual separated X-ray image.

the exponential attenuation of X-rays as they pass through materials.

The proposed method is robust, having successfully separated several areas of real X-ray image data from a double-sided panel of the *Ghent Altarpiece*. Importantly, the results from this image separation also maintain features of the support, such as wood grain and canvas weave, that are not readily apparent in the RGB images used as side information. In the future it will be important to further assess this image separation approach on more challenging sets of X-ray imaging data, such as those with large structural components or other features of interest not apparent at the surface of the painting.

REFERENCES

[1] Janet Lang and Andrew Middleton, "Radiography of cultural material," Routledge, 2005.

[2] D. Bomford (ed.), "Art in the Making: Underdrawings in Renaissance paintings", National Gallery Company, London, 2002.

[3] N. Khandekar, "Preparation of cross-sections from easel paintings", *Studies in Conservation*, vol. 48, pp. 52-64, 2003.

[4] M. Matteini, R. Mazzeo and A. Moles, "Chemistry for Restoration. Painting and Restoration Materials", Nardini, 2016

[5] R. Mazzeo, "Analytical Chemistry for Cultural Heritage", Springer International Publishing, 2017

[6] M. Alfeld and J. A. C. Broekaert, "Mobile depth profiling and sub-surface imaging techniques for historical paintings: a review," *Spectrochimica Acta Part B: Atomic Spectroscopy*, vol. 88, pp. 211–230, 2013.

[7] M. Alfeld and L. de Viguerie, "Recent developments in spectroscopic imaging techniques for historical paintings – a review," *Spectrochimica Acta Part B: Atomic Spectroscopy*, vol. 136, pp. 81–105, 2017.

[8] X. Huang, E. Uffelman, O. Cossairt, M. Walton, and Ag. K. Katsaggelos, "Computational imaging for cultural heritage: Recent developments in spectral imaging, 3-d surface measurement, image relighting, and x-ray mapping," *IEEE Signal Process. Mag.*, vol. 33, no. 5, pp. 130–138, 2016.

[9] Alfeld, M., Pedroso, J.V., van Eikema Hommes, M., Van der Snickt, G., Tauber, G., Blaas, J., Haschke, M., Erler, K., Dik, J., Janssens, K., 2013. "A mobile instrument for in situ scanning macro-XRF investigation of historical paintings". *Journal of Analytical Atomic Spectrometry 28*, 760.

[10] Romano F.P, Caliri C., Nicotra P., Di Martino S., Pappalardo L., Rizzo F. and Santos H.C., "Real-time elemental imaging of large dimension paintings with a novel mobile macro X-ray fluorescence (MA-XRF) scanning technique," *J. Anal. At. Spectrom.*, vol. 32, pp. 773–781, 2017.

[11] Steven Saverwyns, Christina Currie and Eduardo Lamas-Delgado, "Macro X-ray fluorescence scanning (MA-XRF) as tool in the authentication of paintings," *Microchemical Journal*, vol. 137, pp. 139–147, 2018.

[12] Delaney, J.K., Thoury, M., Zeibel, J.G. et al, "Visible and infrared imaging spectroscopy of paintings and improved reflectography", *Herit Sci.*, 4: 6, 2016.

[13] Liang, H., "Advances in multispectral and hyperspectral imaging for archaeology and art conservation", *Appl. Phys. A,* vol. 106, pp. 309–323, 2012.

[14] K.A. Dooley, S. Lomax, J.G. Zeibel, C. Miliani, P. Ricciardi, A. Hoenigswald, M. Loew and J.K. Delaney, "Mapping of egg yolk and animal skin glue paint binders in Early Renaissance paintings using near infrared reflectance imaging spectroscopy", Analyst, vol. 138, pp. 4838-48, 2013.

[15] Legrand, S., Vanmeert, F., Van der Snickt, G., Alfeld, M., De Nolf, W., Dik, J., Janssens, K., 2014. "Examination of historical paintings by state-of-the-art hyperspectral imaging methods: from scanning infra-red spectroscopy to computed X-ray laminography", *Herit Sci.*, 2: 13.

[16] Bruno Cornelis, Ann Dooms, Ingrid Daubechies, and Peter Schelkens. "Report on digital image processing for art historians". In *SAMPTA'09*, pp. Special session, 2009.

[17] B. Cornelis, A. Dooms, J. Cornelis, F. Leen, and P. Schelkens, "Digital painting analysis, at the cross section of engineering, mathematics and culture," in *Proc. Eur. Signal Process. Conf. (EUSIPCO)*, pp. 1254–1258, 2013.

[18] B. Cornelis, Y. Yang, J. T. Vogelstein, A. Dooms, I. Daubechies, and D. Dunson. (2013). "Bayesian crack detection in ultra high resolution multimodal images of paintings." [Online]. Available: https://arxiv.org/abs/1304.5894.

[19] B. Cornelis, T. Ru?i?, E. Gezels, A. Dooms, A. Pi?urica, L. Plati?a, J. Cornelis, M. Martens, M. De Mey and I. Daubechies, "Crack detection and inpainting for virtual restoration of paintings: The case of the Ghent Altarpiece", *Signal Processing*, vol. 93, no. 3, pp. 605-619, 2013.

[20] John K Delaney, Damon M Conover, Kathryn A Dooley, Lisha Glinsman, Koen Janssens, and Murray Loew, "Integrated x-ray fluorescence and diffuse visible-to-near-infrared reflectance scanner for standoff elemental and molecular spectroscopic imaging of paints and works on paper", *Herit Sci.*, vol. 6, no.1, pp. 31, 2018.

[21] Bartosz Grabowski, Wojciech Masarczyk, Przemys?aw G?omb, and Agata Mendys, "Automatic pigment identification from hyperspectral data", *Journal of Cultural Heritage*, vol. 31, pp. 1– 12, 2018.

[22] Neda Rohani, Emeline Pouyet, Marc Walton, Oliver Cossairt, and Aggelos K Katsaggelos, "Nonlinear unmixing of hyperspectral datasets for the study of painted works of art", *Angewandte Chemie*, vol. 130, no. 34, pp. 11076–11080, 2018

[23] Balas, C., Epitropou, G., Tsapras, A. et al, "Hyperspectral imaging and spectral classification for pigment identification and mapping in paintings by El Greco and his workshop," *Multimed. Tools Appl.*, vol. 77, pp. 9737, 2018.

[24] Sina Jafarpour, Gungor Polatkan, Eugene Brevdo, Shannon Hughes, Andrei Brasoveanu, and Ingrid Daubechies, "Stylistic analysis of paintings using wavelets and machine learning", in *Signal Processing Conference*, 2009 17th European, pp. 1220–1224. IEEE, 2009.

[25] C Richard Johnson, Ella Hendriks, Igor Berezhnoy, Eugene Brevdo, Shannon Hughes, Ingrid Daubechies, Jia Li, Eric Postma, and James Z. Wang, "Image processing for artist identification computerized analysis

of Vincent van Goghs painting brushstrokes", *IEEE Signal Process. Mag.*, July 2008.
[26] C. R. Johnson et al., "Image processing for artist identification," *IEEE Signal Process. Mag.*, vol. 25, no. 4, pp. 37–48, Jul. 2008.
[27] N. van Noord, E. Hendriks, and E. Postma, "Toward discovery of the artist's style: Learning to recognize artists by their artworks," *IEEE Signal Process. Mag.*, vol. 32, no. 4, pp. 46–54, Jul. 2015.
[28] B. Cornelis, H. Yang, A. Goodfriend, N. Ocon, J. Lu, and I. Daubechies, "Removal of Canvas Patterns in Digital Acquisitions of Paintings," *IEEE Trans. Image Process.*, vol. 26, no. 1, pp. 160-171, 2017.
[29] Joseph Padfield, David Saunders, John Cupitt, and Robert Atkinson, "Improvements in the acquisition and processing of x-ray images of paintings," National Gallery Technical Bulletin, vol. 23, pp. 62–75, 2002.
[30] Rujie Yin, David Dunson, Bruno Cornelis, Bill Brown, Noelle Ocon, and Ingrid Daubechies, "Digital cradle removal in x-ray images of art paintings", in *ICIP*, pp. 4299–4303, 2014.
[31] EE. L. van der Maaten and R. Erdmann, "Automatic thread-level canvas analysis: A machine-learning approach to analyzing the canvas of paintings," *IEEE Signal Process. Mag.*, vol. 32, no. 4, pp. 38–45, Jul. 2015.
[32] H. Yang, J. Lu, W. Brown, I. Daubechies, and L. Ying, "Quantitative canvas weave analysis using 2-D synchrosqueezed transforms: Application of time-frequency analysis to art investigation," *IEEE Signal Process. Mag.*, vol. 32, no. 4, pp. 55–63, Jul. 2015.
[33] Anitha A., Brasoveanu A., Duarte M., Hughes S., Daubechies I., Dik J., Janssens K., Alfeld M., "Restoration of X-ray fluorescence images of hidden paintings," *Signal Process.*, 4299–4303, 2014.
[34] Jan Blazek, Oldrich Vlasic and Barbara Zitova, "Improvement of the visibility of concealed features in misregistered nir reflectograms by deep learning", in *IOP Conference Series: Materials Science and Engineering*, vol. 364, pp. 012058, 2018.
[35] David Thurrowgood, David Paterson, Martin D De Jonge, Robin Kirkham, Saul Thurrowgood, and Daryl L Howard, "A hidden portrait by Edgar Degas," *Scientific reports*, 6:29594, 2016.
[36] Sober, Barak, Spike Bucklow, Nathan Daly, Ingrid Daubechies, Pier Luigi Dragotti, Catherine Higgitt, Jun-Jie Huang, Aleksandra Piz˘urica, Miguel R D Rodrigues, and Su Yan. 'Revealing and Reconstructing Hidden or Lost Features in Art Investigation'. IEEE BITS the Information Theory Magazine, 2022, 16.
[37] Casali, F., "X-ray and neutron digital radiography and computed tomography for cultural heritage". Physical Techniques in the Study of Art, Archaeology and Cultural Heritage, 41–123, 2006.
[38] D. Gavrilov, R.Gr. Maev, and D.P. Almond, "A review of imaging methods in analysis of works of art: Thermographic imaging method in art analysis", *Can. J. Phys.*, vol. 92, pp. 341–364, 2014.
[39] A. Hyvarinen, J. Karhunen, and E. Oja, Independent Component Analysis, vol. 46. New York, NY, USA: Wiley, 2004.
[40] A. Hyvarinen, "Gaussian moments for noisy independent component analysis," *IEEE Signal Process. Lett.*, vol. 6, no. 6, pp. 145–147, Jun. 1999.
[41] Po-Sen Huang, Scott Deeann Chen, Paris Smaragdis, and Mark Hasegawa-Johnson, "Singing-voice separation from monaural recordings using robust principal component analysis," in *ICASSP*, 2012.
[42] Tak-Shing Chan, Tzu-Chun Yeh, Zhe-Cheng Fan, Hung-Wei Chen, Li Su, Yi-Hsuan Yang, and Roger Jang, "Vocal activity informed singing voice separation with the ikala dataset," in *ICASSP*, 2015.
[43] Antoine Liutkus, Derry Fitzgerald, Zafar Rafii, Bryan Pardo, and Laurent Daudet, "Kernel additive models for source separation," *IEEE Trans. Signal Process.*, vol. 62, no. 16, pp. 4298–4310, 2014.
[44] J. Bobin, J.-L. Starck, J. Fadili, and Y. Moudden, "Sparsity and morphological diversity in blind source separation," *IEEE Trans. Image Process.*, vol. 16, no. 11, pp. 2662–2674, Nov. 2007.
[45] J.-L. Starck, M. Elad, and D. Donoho, "Redundant multiscale transforms and their application for morphological component separation," *Adv. Imag. Electron Phys.*, vol. 132, pp. 287–348, 2004.
[46] J. Bobin, Y. Moudden, J. L. Starck, and M. Elad, "Morphological diversity and source separation," *IEEE Signal Process. Lett.*, vol. 13, no. 7, pp. 409–412, Jul. 2006.
[47] Po-Sen Huang, Minje Kim, Mark Hasegawa-Johnson, and Paris Smaragdis, "Deep learning for monaural speech separation," in *ICASSP*, 2014.
[48] Dong Yu, Morten Kolb?k, Zheng-Hua Tan, and Jesper Jensen, "Permutation invariant training of deep models for speaker-independent multi-talker speech separation," in *ICASSP*, 2017.
[49] Tavi Halperin, Ariel Ephrat, and Yedid Hoshen, "Neural separation of observed and unobserved distributions," arXiv, 2018.
[50] Y. Hoshen, "Towards Unsupervised Single-channel Blind Source Separation Using Adversarial Pair Unmix-and-remix," in *ICASSP*, Brighton, United Kingdom, 2019, pp. 3272-3276.
[51] Ian Goodfellow, Jean Pouget-Abadie, Mehdi Mirza, Bing Xu, David Warde-Farley, Sherjil Ozair, Aaron Courville, and Yoshua Bengio, "Generative adversarial nets," in *NIPS*, 2014.
[52] Closer to Van Eyck. http://closertovaneyck.kikirpa.be/ghentaltarpiece. Accessed: 2019-01-17.
[53] Aleksandra Pizurica, Ljiljana Platisa, Tijana Ruzic, Bruno Cornelis, Ann Dooms, Maximil-iaan Martens, Helene Dubois, Bart Devolder, Marc De Mey, and Ingrid Daubechies, "Digitalimage processing of the ghent altarpiece: Supporting the painting's study and conservation treatment," *IEEE Signal Process. Magazine*, 32(4):112–122, 2015.
[54] B. Cornelis et al., "Crack detection and inpainting for virtual restoration of paintings: The case of the Ghent Altarpiece," *Signal Process.*, vol. 93, no. 3, pp. 605–619, 2012.
[55] N. Deligiannis, J. F. C. Mota, B. Cornelis, M. R. D. Rodrigues and I. Daubechies, "Multi-Modal Dictionary Learning for Image Separation With Application in Art Investigation," *IEEE Trans. Image Process.*, vol. 26, no. 2, pp. 751-764, Feb. 2017.
[56] Z. Sabetsarvestani, B. Sober, C. Higgitt, I. Daubechies, and M. R. D. Rodrigues, "Artificial intelligence for art investigation: Meeting the challenge of separating X-ray images of the Ghent Altarpiece," *Science Advances*, vol. 5, no. 8, pp. 751-764, 2019.
[57] Z. Sabetsarvestani, F. Renna, F. Kiraly, and M. R. D. Rodrigues, "Source Separation with Side Information Based on Gaussian Mixture Models With Application in Art Investigation," *IEEE Trans. Signal Process.* (to appear).
[58] W. Pu, B. Sober, N. Daly, C. Higgitt, I. Daubechies and M. R. D. Rodrigues, "A Connected Auto-Encoders Based Approach for Image Separation with Side Information: With Applications to Art Investigation," in *ICASSP*, 2020.
[59] V. Monga, Y. Li, Y. C. Eldar, "Algorithm Unrolling: Interpretable, Efficient Deep Learning for Signal and Image Processing." [Online]. Available: https://arxiv.org/abs/1912.10557?context=cs, 2020.
[60] Gu J , Wang Z , Kuen J , et al, "Recent Advances in Convolutional Neural Networks," *Pattern Recognition*, 2015.
[61] Plaut, E. , and R. Giryes, "Learned Convolutional Sparse Coding," in *ICASSP*, 2018.
[62] G. Heitz, and G. Chechik, "Object separation in X-ray image sets," in *CVPR*, 2010.
[63] M. Baur, N. Uhlmann and T. Poschel, "Correction of beam hardening in X-ray radiograms," [Online]. Available: https://arxiv.org/pdf/1811.04102.pdf, 2022.
[64] W. Souidène, A. Bey, K. Abed-Meraim, and A. Beghdadi, "Blind Image Separation using Sparse Representation," in *IEEE International Conference on Image Processing (ICIP)*, San Antonio, United States. pp.125–128, 2007.
[65] X. Yu, J. Xu, D. Hu, and H. Xing, "A new blind image source separation algorithm based on feedback sparse component analysis," *Signal Process.*, vol. 93, no. 1, pp. 288–296, 2013.
[66] Y. Zhao, L. Wang, and Y. Han, "The restoration of x-ray radiograph based on ICA," *Nucl. Instrum. Methods Phys. Res., Sect. A*, vol. 614, no. 2, pp. 227–230, 2010.